High-Fidelity Multidisciplinary Sensitivity Analysis Framework for Multipoint Rotorcraft Optimization

Li Wang * Boris Diskin†
National Institute of Aerospace, Hampton, VA, USA
Robert T. Biedron ‡ Eric J. Nielsen §
NASA Langley Research Center, Hampton, VA, USA
Valentin Sonneville ¶ Olivier A. Bauchau ‖
University of Maryland, MD, USA

A multidisciplinary, gradient-based sensitivity-analysis methodology is evaluated for optimization of rotorcraft configurations. The tightly coupled discipline models include physics-based fluid dynamics and rotorcraft comprehensive analysis. A discretely-consistent adjoint method accounts for sensitivities of the unsteady flow and unstructured, dynamic, overset grids, while sensitivities of structural responses to aerodynamic loads are computed using a complex-variable method. The methodology is applied to optimize the shape of UH-60A Blackhawk helicopter blades for hover and forward flight conditions. The objective of the multipoint design is to simultaneously increase the rotorcraft figure of merit in a hover flight and reduce the rotor power in a forward flight. Trimmed loose-coupling solutions for the baseline configuration are used to initiate the tight-coupling multidisciplinary analysis. Target thrust and rolling and pitching moments are enforced as optimization constraints. The optimized configuration improves the optimization metrics at both design points. The improved performance and all constraints are maintained over many revolutions beyond the optimization interval, satisfying the required flight conditions. Computational cost of the optimization cycle is assessed in a high-performance computing environment and found affordable for design of rotorcraft in general level-flight conditions.

I. Introduction

In the last several decades, comprehensive analysis (CA) tools[1–3] have been used extensively in the helicopter industry for aeromechanic analysis and design. These tools are computationally efficient, but rely on low-fidelity aerodynamic models, such as lifting-line and vortex-wake models. These models cannot adequately predict complex aerodynamic phenomena such as turbulence, boundary-layer separation, shock-wave interactions, dynamic stall, etc. To account for complicated three-dimensional effects and compressibility of the flow field, state-of-the-art high-fidelity rotorcraft simulations couple a CA model with a physics-based computational fluid dynamics (CFD) model.[4–8]

While high-fidelity CFD/CA coupled rotorcraft analysis has been the focus in many studies, design optimization methodologies based on high-fidelity rotorcraft analysis received relatively little attention. The main obstacle in the way of applying such methodology for practical design is a high computational cost. A multidisciplinary analysis for

*Senior Research Engineer, AIAA Member, li.wang@nianet.org
†Research Fellow, AIAA Associate Fellow, bdiskin@nianet.org
‡Research Scientist, robert.t.biedron@nasa.gov
§Research Scientist, AIAA Associate Fellow, eric.j.nielsen@nasa.gov
¶Assistant Research Scientist, vspsonn@umd.edu
‖Professor, AIAA Fellow, obauchau@umd.edu

typical rotorcraft conditions requires many thousands of computational hours and can be conducted only in a high-performance computing environment. Traditional sensitivity analysis methods based on finite-difference approaches require at least one dedicated simulation to compute sensitivity with respect to a single design parameter. A relevant rotorcraft configuration involves hundreds of design parameters. Finite-difference sensitivity analysis methods become prohibitive for such applications. A high computational cost also limits applications of gradient-free methods such as genetic algorithms, which can be applied for optimization of CA models, but are not affordable for optimization of high-fidelity computational models with many design parameters. Adjoint-based sensitivity analysis is enabling for applications characterized by many design parameters and few objectives. Adjoint methods compute sensitivities of an objective function with respect to many design parameters for a computational cost that is similar to the cost of a single simulation. Recent advances in the adjoint-based sensitivity analysis methodology coupled with advances in high-performance computing pave the way for high-fidelity multidisciplinary sensitivity analysis and design optimization for rotorcraft applications.[8–14]

In this paper, a discretely-consistent, adjoint-based, multidisciplinary sensitivity analysis is presented for high-fidelity, tightly-coupled CFD/CA simulations. A highly-scalable, unstructured-grid CFD solver, FUN3D,[5,15] and a nonlinear, flexible, multibody-dynamics CA solver, DYMORE,[3] are coupled to predict the airloads and structural responses of helicopter rotor blades. A discretely-consistent, adjoint-based sensitivity analysis available in FUN3D provides sensitivities of turbulent flows and unstructured, dynamic, deforming, overset grids, while a complex-variable perturbation approach[16] is used to compute sensitivities of DYMORE solutions with respect to aerodynamic loads. The multidisciplinary sensitivity analysis integrates all sensitivity components of the coupled system.

Previous papers[7,12,13] reported on coupling of earlier DYMORE models with FUN3D for analysis and design optimization. Recent publications[8,17] presented FUN3D coupling with a new, highly optimized model, denoted as DYMORE5. DYMORE5 employs a local-frame motion formalism[18–20] for simulation of rotor dynamics. The motion formalism reduces nonlinearity of the motion equations and results in nearly constant iteration matrices, thereby avoiding costly factorization at each time step. A domain-decomposition technique has also been developed in DYMORE5, which enables the use of OpenMP and Message Passing Interface libraries for parallel computing. These DYMORE5 capabilities lead to significant reductions in computing time without compromising accuracy. Efficient methodology for multidisciplinary optimization of a coupled FUN3D/DYMORE5 system has been developed and applied for optimization of HART-II rotorcraft configuration in a descent flight.[8]

In the current work, the sensitivity analysis capabilities of the coupled FUN3D/DYMORE5 system have been further extended and evaluated for multipoint design and optimization of UH-60A Blackhawk helicopter blades. Specifically, the first design point represents a hover flight condition and the second design point represents a high-speed forward flight with advancing-blade negative lift. The objective of the multipoint design is to simultaneously maximize the figure of merit (FM) for the hover flight and reduce the rotor power for the forward flight. Each design point targets certain thrust and rolling and pitching moments as optimization constraints.

The organization of the paper is as follows. Section II describes the CFD and CA solvers used in this work. The mathematical formulation of the multidisciplinary sensitivity analysis in Section III is followed by presentation of the design optimization framework in Section IV. In Section V, the coupled CFD/CA analysis is verified and validated through comparisons of the FUN3D/DYMORE5 simulations with established computational solutions and experimental measurements for a UH-60A rotor in both hover and high-speed flight conditions. Section VI demonstrates a constrained, gradient-based, two-point design optimization for the UH-60A rotor system. The computational cost of individual components of the design optimization cycle is analyzed. Section VII concludes with a summary.

II. CFD and CA Solvers

The flow solver used in this study is FUN3D[15] developed and supported by the NASA Langley Research Center. FUN3D is a finite-volume, node-centered, unstructured-grid Reynolds-averaged Navier-Stokes (RANS) solver, which is widely used for high-fidelity analysis and adjoint-based optimization of complex turbulent flows.[5,8–10,21–23] FUN3D solves the governing flow equations on tetrahedral or mixed-element grids. At median dual-control-volume faces, the inviscid fluxes are computed by Roe's scheme.[24] For second-order accuracy, solutions at dual faces are obtained by a UMUSCL (Unstructured Monotonic Upstream-centered Scheme for Conservation Laws) scheme.[25,26] The viscous fluxes are discretized using a finite-volume formulation, in which the Green-Gauss theorem is applied to compute

gradients on dual faces for tetrahedral meshes. For nontetrahedral meshes, the cell-based Green-Gauss gradients are augmented with edge-based gradients to improve the h-ellipticity of viscous operators.[27] The diffusion term in the turbulence model is discretized in the same fashion as the viscous terms in the flow equations. The vorticity-based source term for the turbulence model is computed by using velocity gradients evaluated by the Green-Gauss method on dual volumes. To advance the flow solutions in time, a library of time integration schemes is available including standard first-order and second-order backward difference schemes known as BDF1 and BDF2 schemes, respectively, as well as a blended second- and third-order backward difference scheme, referred to as BDF2opt.[28] For overset grids, the DiRTlib[29] and SUGGAR++[30] codes are used for communication between components of the mesh.

The CA code is a nonlinear, flexible, multibody-dynamics code, DYMORE,[3] which provides static, dynamic, stability, and trim analyses of rotorcraft configurations. DYMORE contains libraries of primitive elements such as rigid bodies, mechanical joints, elastic springs, dampers, beams, shells, and plates. The internal aerodynamics model in DYMORE is a low-fidelity approximation based on lifting-line theory. For this study, the new DYMORE5 model[18–20] has been employed. DYMORE5 is capable of operating in both real and complex modes. The complex-mode operation is achieved by replacing all real-valued variables in the code with complex-valued variables and overwriting the real-valued functions and operators with corresponding complex-valued functions and operators. Sensitivities of DYMORE5 solutions can be evaluated through complex-variable analysis.[12,16] Unlike a real-valued finite-difference approach, the complex-variable sensitivity calculations do not suffer from subtractive cancellation errors,[16,31,32] thereby increasing accuracy and robustness.

A FUN3D/DYMORE5 interface has been developed to exchange aerodynamic loads and structural deflections between high-fidelity aero and structural dynamics models.[33] This interface has been extended to enable multidisciplinary sensitivity analysis that integrates adjoint-based CFD sensitivities and complex-variable CA sensitivities.[8,12,13] The extended multidisciplinary system can conduct CFD/CA simulations based on loosely or tightly coupled approaches.[4,5,8,12] The multidisciplinary analysis and design optimization framework has been developed based on the tightly coupled approach, where FUN3D executes the DYMORE5 routines directly using the interface; all required force-and-displacement data are transferred in memory at each time step, resulting in efficient and fast data exchange.

III. Mathematical Formulations

Mathematical formulations for a tightly coupled multidisciplinary CFD/CA analysis and the corresponding sensitivity analysis are outlined in this section. More detailed descriptions of the formulations can be found elsewhere.[13]

In the coupled system, a CA solution vector at time level n, denoted as $\mathbf{u}^n$, describes linear and angular displacements at specified airstations along the quarter-chord line of the rotor blade. The blade displacements represent combined rigid (such as blade pitching, flapping, and/or lead-lagging) and elastic motions. The blade azimuthal rotation is represented separately by rigid motions of the blade component grids from the reference frame to the position and orientation corresponding to time level n.[13] The CA solution is used to update the CFD surface grid, $\mathbf{X}_s^n$, expressed as

$$\mathbf{X}_s^n = \mathbf{T}_s^n(\mathbf{u}^n)\hat{\mathbf{X}}_s(\mathbf{D}), \tag{1}$$

where $\mathbf{T}_s^n$ denotes a transform matrix for elastic surface motion at time step n. The matrix varies at individual surface nodes and depends on the DYMORE5 solutions, $\mathbf{u}^n$. The reference surface grid, $\hat{\mathbf{X}}_s$, is obtained based on a surface parameterization and explicitly depends on the design (shape) parameters, $\mathbf{D}$. The reference surface grid is not affected by elastic deformations or rigid motions. To minimize volume-grid deformation, the CFD code uses the CA displacements, $\mathbf{u}^n$, to compute average pitch, flap, and lead-lag angles for each rotor blade. A rigid rotation motion based on these angles is applied to the blade component grid to keep the elastically-deformed blade centered within the component grid.[13] This approach improves robustness of the mesh deformation process when large flapping motions are present.[33] A vector of CFD solutions, $\mathbf{Q}^n$, is computed on the composite, overset volume grid, $\mathbf{X}^n$, at time level n. A vector of airloads, $\mathbf{f}^n$, is computed by the CFD code using a boundary slicing procedure at time level n. In the boundary slicing procedure, a piecewise-linear closed contour is identified for each airstation. The contour is composed of connected linear segments cutting specific faces of the unstructured boundary grid. The sectional force components are obtained by integrating the pressure and viscous-force contributions over this contour; the sectional moments are computed by multiplying the integrated segment forces with the relative distance to the quarter chord. The computation of sectional airloads is denoted as $\mathbf{f}^n = \mathbf{S}^n(\mathbf{Q}^n, \mathbf{X}^n)$, where $\mathbf{S}^n$ represents the boundary slicing. The

sectional airloads are transferred from the CFD code to the CA code to compute structural responses. The transfer procedure used in the current multidisciplinary simulations is similar to the previously implemented FUN3D/DYMORE interface[33] and follows the procedure used in FUN3D/CAMRAD simulations.[5,7] The following equations for a tight-coupling formulation are written in the order in which the equations are solved. Here, the BDF1 scheme is used for simplicity of the presentation.

$$\text{Reference Grid}: \hat{\mathbf{G}}(\hat{\mathbf{X}}, \hat{\mathbf{X}}_s, \mathbf{D}) = \mathbf{0}, \tag{2}$$

$$\text{Initial Grid}: \mathbf{G}^0(\mathbf{X}^0, \hat{\mathbf{X}}, \mathbf{T}_r^0(\mathbf{u}^0), \mathbf{D}) = \mathbf{0}, \tag{3}$$

$$\text{Initial Flow}: \mathbf{R}^0(\mathbf{Q}^0, \overline{\mathbf{Q}}(\mathbf{D})) = \mathbf{0}, \tag{4}$$

$$\text{Initial Load}: \mathbf{F}^0(\mathbf{f}^0,\ \mathbf{Q}^0, \mathbf{X}^0) = \mathbf{0}, \tag{5}$$

$$\text{CA}: \mathbf{C}^n(\mathbf{u}^n, \mathbf{u}^{n-1}, \mathbf{f}^{n-1}, \mathbf{D}) = \mathbf{0}, \tag{6}$$

$$\text{CFD Grid}: \mathbf{G}^n(\mathbf{X}^n, \mathbf{T}_r^n(\mathbf{u}^n), \mathbf{X}_s^n(\mathbf{u}^n), \hat{\mathbf{X}}, \mathbf{D}) = \mathbf{0}, \tag{7}$$

$$\text{CFD Flow}: \mathbf{R}^n(\mathbf{Q}^n, \mathbf{Q}^{n-1}, \mathbf{X}^n, \mathbf{X}^{n-1}, \mathbf{D}) = \mathbf{0}, \tag{8}$$

$$\text{Loads}: \mathbf{F}^n(\mathbf{f}^n, \mathbf{Q}^n, \mathbf{X}^n) = \mathbf{0}, \tag{9}$$

where $\hat{\mathbf{X}}$ represents the reference volume grid accommodating the surface mesh displacements due to changes in design variables; $\mathbf{u}^0$ represents an initial CA solution at time level $n = 0$ for the tight-coupling analysis; $\mathbf{T}_r^n$ is a transform matrix representing the rigid motion based on the average angles computed from the DYMORE5 solutions, $\mathbf{u}^n$; $\overline{\mathbf{Q}}$ represents a given initial flow condition; and the superscript index n denotes the time step in the range of $1 \le n \le N$, where N is the total number of time steps. Equation (9) represents the sectional airloads computation that is expressed as $\mathbf{F}^n \equiv \mathbf{f}^n - \mathbf{S}^n(\mathbf{Q}^n, \mathbf{X}^n) = \mathbf{0}$. In the current implementation, the initial conditions, $\mathbf{u}^0$ and $\overline{\mathbf{Q}}$, are taken from a trimmed solution of a preliminary loose-coupling analysis of the baseline configuration.

In the sensitivity analysis framework presented here, the CFD flow, CFD grid, and the load equations use adjoint formulations, whereas sensitivities of the surface grid and the extracted rigid motion to the aerodynamic loads are computed by a complex-variable perturbation method.[16] The sensitivity of an objective function to design parameters is computed by differentiating a Lagrangian functional, L, formed as

$$L = f(\mathbf{Q}, \mathbf{u}, \mathbf{X}, \mathbf{f}, \mathbf{D}) + \sum_{n=0}^{N} [\mathbf{\Lambda}_R^n]^T \mathbf{R}^n + \sum_{n=0}^{N} [\mathbf{\Lambda}_G^n]^T \mathbf{G}^n + \sum_{n=0}^{N} [\mathbf{\Lambda}_F^n]^T \mathbf{F}^n + \left[\mathbf{\Lambda}_{\hat{G}}\right]^T \hat{\mathbf{G}}, \tag{10}$$

where $f(\mathbf{Q}, \mathbf{u}, \mathbf{X}, \mathbf{f}, \mathbf{D})$ is a general objective function; $\mathbf{Q}$, $\mathbf{u}$, $\mathbf{X}$, and $\mathbf{f}$ represent CFD solutions, CA surface displacements, grids, and airloads solutions at all time levels, respectively; $\mathbf{\Lambda}_R$, $\mathbf{\Lambda}_G$, and $\mathbf{\Lambda}_F$ are vectors of the time-dependent adjoint solutions for the flow, grid, and load equations, respectively; $\mathbf{\Lambda}_{\hat{G}}$ denotes the adjoint solution for the reference-grid equation; and the superscript T represents the transposition operator. Differentiating the Lagrangian with respect to design parameters $\mathbf{D}$ and equating the coefficients of state-variable sensitivities to zero[34] yields the following adjoint equations:

$$\text{Load}: \left[\frac{\partial f}{\partial \mathbf{f}^n}\right] + [\mathbf{\Lambda}_F^n]^T \left[\frac{\partial \mathbf{F}^n}{\partial \mathbf{f}^n}\right] + \sum_{k=n+1}^{N} \left[\mathbf{\Lambda}_G^k\right]^T \left[\frac{\partial \mathbf{G}^k}{\partial \mathbf{f}^n}\right] = \mathbf{0}, \tag{11}$$

$$\text{Flow}: \left[\frac{\partial f}{\partial \mathbf{Q}^n}\right] + \sum_{j=n}^{n+1} \left[\mathbf{\Lambda}_R^j\right]^T \left[\frac{\partial \mathbf{R}^j}{\partial \mathbf{Q}^n}\right] + [\mathbf{\Lambda}_F^n]^T \left[\frac{\partial \mathbf{F}^n}{\partial \mathbf{Q}^n}\right] = \mathbf{0}, \tag{12}$$

$$\text{Grid}: \left[\frac{\partial f}{\partial \mathbf{X}^n}\right] + [\mathbf{\Lambda}_G^n]^T \left[\frac{\partial \mathbf{G}^n}{\partial \mathbf{X}^n}\right] + \sum_{j=n}^{n+1} \left[\mathbf{\Lambda}_R^j\right]^T \left[\frac{\partial \mathbf{R}^j}{\partial \mathbf{X}^n}\right] + [\mathbf{\Lambda}_F^n]^T \left[\frac{\partial \mathbf{F}^n}{\partial \mathbf{X}^n}\right] = \mathbf{0}, \tag{13}$$

$$\text{Reference Grid}: \left[\mathbf{\Lambda}_{\hat{G}}\right]^T \left[\frac{\partial \hat{\mathbf{G}}}{\partial \hat{\mathbf{X}}}\right] + \sum_{m=0}^{N} [\mathbf{\Lambda}_G^m]^T \left[\frac{\partial \mathbf{G}^m}{\partial \hat{\mathbf{X}}}\right] = \mathbf{0}. \tag{14}$$

The adjoint equations are solved in the reverse order in time, starting from time step $n = N$ and proceeding to time step $n = 0$. Equations (11)−(13) are subject to the following conditions: $\mathbf{\Lambda}_G^{N+1} = 0$ and $\mathbf{\Lambda}_R^{N+1} = 0$. Note that an adjoint

formulation for the CA model is not yet available, therefore, the CA equations are not included in the Lagrangian. The CA equations are used to establish the direct relationships between airloads $\mathbf{f}$ at a time level and CA states $\mathbf{u}$ at all subsequent time levels. Sensitivities of CA solutions to airloads are assessed by the complex-variable perturbation method. The linearization term $[\partial \mathbf{G}^k/\partial \mathbf{f}^n]$ in Eq. (11) denotes sensitivities of the CFD grid at time level k to aerodynamic loads at time level n. The implementation of this term treats the CA states $\mathbf{u}$ as internal variables and accounts for all sensitivities from the CA fields through CFD grid-motion sensitivities. The partial derivatives of grid motions with respect to $\mathbf{u}$ are taken based on the functional dependencies between the grid motions and CA states defined in Eq. (7). Consequently, the grid motion sensitivities with respect to airload perturbations are computed using the chain rule as

$$\left[\frac{\partial \mathbf{G}^k}{\partial \mathbf{f}^n}\right] = \left\{ \left[\frac{\partial \mathbf{G}^k}{\partial \mathbf{T}_r^k}\right]\left[\frac{\partial \mathbf{T}_r^k}{\partial \mathbf{u}^k}\right] + \left[\frac{\partial \mathbf{G}^k}{\partial \mathbf{X}_s^k}\right]\left[\frac{\partial \mathbf{X}_s^k}{\partial \mathbf{u}^k}\right] \right\} \left[\frac{\partial \mathbf{u}^k}{\partial \mathbf{f}^n}\right], \tag{15}$$

where $[\partial \mathbf{u}^k/\partial \mathbf{f}^n]$ denotes sensitivities of DYMORE5 solutions at time level k to aerodynamic loads at time level n. The terms $[\partial \mathbf{G}^k/\partial \mathbf{T}_r^k]$ and $[\partial \mathbf{G}^k/\partial \mathbf{X}_s^k]$ are manually differentiated. To assess $[\partial \mathbf{u}^k/\partial \mathbf{f}^n]$, an airload component at time level n is perturbed by $i10^{-50}$, and the complex-variable DYMORE5 solutions $\mathbf{u}^k$ are computed for subsequent time levels k, $n+1 \le k \le N$. The real part of $\mathbf{u}^k$ is identical to that computed in the forward CFD/CA analysis, while the imaginary part (divided by 10^{-50}) is the sensitivity of $\mathbf{u}^k$ to the particular airload component. The assessment of sensitivities of DYMORE5 solutions to aerodynamic loads is performed in parallel. The sensitivities of rigid motion and elastic surface grids to DYMORE5 solutions, $[\partial \mathbf{T}_r^k/\partial \mathbf{u}^k]$ and $[\partial \mathbf{X}_s^k/\partial \mathbf{u}^k]$ in Eq. (15), are also computed by complex-variable analysis. Each component of the DYMORE5 solutions is perturbed with $i10^{-50}$ to assess the corresponding sensitivities. These computations are confined to time level k and also performed in parallel.

From Eq. (11), the computational time of evaluating sensitivities of all CFD grids to all airload components is quadratically proportional to the number of time steps, linearly proportional to the number of airload components (or, equivalently, DYMORE5 solution components) at a time level, and inversely proportional to the number of processors used in the complex-variable sensitivity analysis. In the present work, the number of processing cores is selected to be the same as the number of airload components at a time level. This selection removes the linear dependence of the execution time on the number of airload components.

The final multidisciplinary sensitivity derivatives are computed as

$$\frac{dL}{d\mathbf{D}} = \left[\frac{\partial f}{\partial \mathbf{D}}\right] + \sum_{n=0}^{N} [\mathbf{\Lambda}_R^n]^T \left[\frac{\partial \mathbf{R}^n}{\partial \mathbf{D}}\right] + \sum_{n=0}^{N} [\mathbf{\Lambda}_G^n]^T \left[\frac{\partial \mathbf{G}^n}{\partial \mathbf{D}}\right] + \left[\mathbf{\Lambda}_{\hat{G}}\right]^T \left[\frac{\partial \hat{\mathbf{G}}}{\partial \mathbf{D}}\right]. \tag{16}$$

Verification of this sensitivity analysis framework is provided elsewhere.[13]

IV. Design Optimization Cycle

A sequential quadratic-programming optimizer, SNOPT,[35,36] is used to drive the gradient-based, multipoint rotorcraft design optimization for N_p flight conditions. The design optimization cycle is illustrated in Fig. 1 and summarized as the following seven steps.

1. Subcycle iterations over design points are conducted for the baseline configuration and initial design parameters. For each design point, tight-coupling CFD/CA solutions are computed. The values of the specific objective and corresponding constraints are evaluated.

2. Subcycle adjoint iterations over design points are conducted. At each design point, the multidisciplinary adjoint equations are solved by marching in reverse time. The latest available design parameters and the corresponding CFD flow, CFD grid, and CA solutions are used. The sensitivities of the objective and constraints to desired design parameters are evaluated.

3. The optimizer, SNOPT, is provided with the current values of the objectives and constraints, the current values of the design parameters, the sensitivities of the objectives and constraints to the design parameters, as well as lower and upper bounds of the design parameters, from all design points.

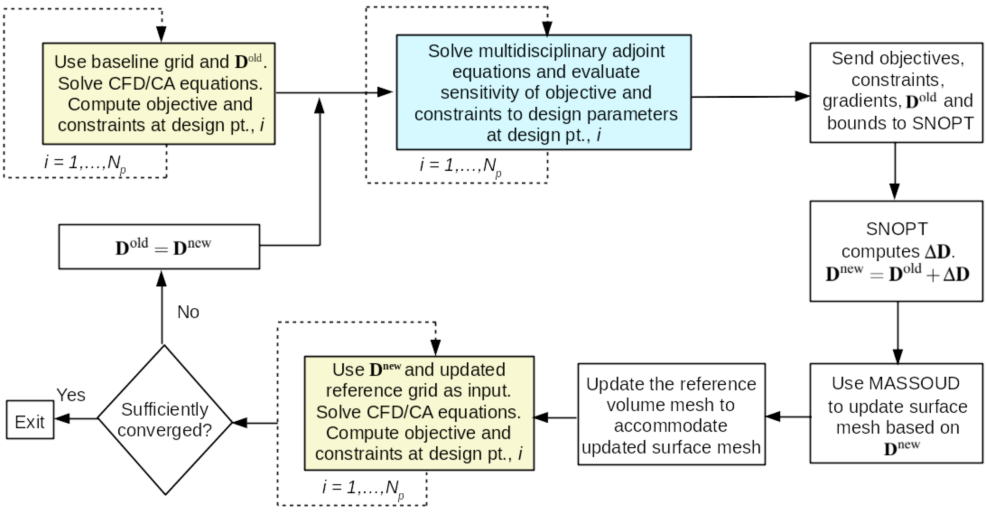

Figure 1. Flowchart illustrating multipoint design optimization cycle.

4. SNOPT provides corrections for the design parameters. Those corrections are applied to compute new design parameters.
5. The surface grid is updated using new shape design parameters.
6. The CFD volume grid is updated by using a linear elasticity approach.
7. Subcycle iterations over design points are conducted using the new design parameters. For each design point, tight-coupling CFD/CA solutions are computed. The values of the specific objective and corresponding constraints are evaluated.
8. Steps of $2-7$ are repeated until the objective function at each design point is sufficiently improved, and constraints are converged to a satisfactory level.

V. FUN3D/DYMORE Loose-Coupling Analysis

In this section, verification and validation of loosely coupled FUN3D/DYMORE5 analysis[13] is conducted for an isolated UH-60A rotor in hover and forward flight. The multidisciplinary analyses of loosely and tightly coupled FUN3D/DYMORE systems have been previously verified and validated for a HART-II test model[7,8,12,13] in descent flight with significant blade-vortex interactions. The multidisciplinary analysis of the UH-60A test model requires modeling of a fully articulated rotor system, hinge and blade motions, as well as capturing of three-dimensional, unsteady, transonic aerodynamic phenomena.

The test conditions and rotor parameters are summarized in Table 1 for the two level-flight data points considered in this paper. Other important test parameters can be found elsewhere.[4,37] Figure 2(a) illustrates the UH-60A blade planform geometry and radial stations where flight-test measurements are available. Two (coarse and fine) composite, unstructured, tetrahedral, overset grids are used for the CFD flow simulations; each composite grid consists of four blade component grids and a stationary background grid. The coarse composite grid contains a total of 6,842,485 nodes and 40,347,585 tetrahedral elements. The fine composite grid contains 17,569,918 nodes and 103,450,109 tetrahedral elements for higher resolution. Figure 2(b) shows the coarse overset grid; an overview of the blade component grids is shown in the low-right corner. These grids were originally developed for a forward-flight analysis, where the wake propagates downstream, but does not propagate far in the vertical direction. These grids are suboptimal for hover-flight conditions, where the wake extends far below the rotor disk. The RANS equations with the standard Spalart-Allmaras (SA) turbulence model[38] are used in the CFD flow simulations. The BDF2opt temporal scheme is used to advance in

Table 1. UH-60A rotor test parameters.

Parameter	Hover flight	High-speed forward flight (C8534)
Solidity-weighted thrust coefficient, C_T/σ	0.05, 0.07 (C9605), 0.09	0.081
Rotor rolling moment coefficient, C_{mx}	0	0.000091
Rotor pitching moment coefficient, C_{my}	0	-0.000063
Rotor shaft angle, α_S	0°	0°
Tip Mach No., M_{tip}	0.650	0.642
Advance ratio, μ	0	0.3645
Flow angle of attack, α	0°	-7.31°
Freestream speed of sound, a_∞	1117.0 ft/s	1130.3 ft/s
Freestream air density, ρ_∞	0.002378 slug/s	0.002028 slug/s
Rotor rotational speed, Ω	258.4 rpm	258.1 rpm
Rotor solidity, σ	0.0826	0.0826
Blade radius, R	26.833 ft	26.833 ft
Blade reference chord length, c_{ref}	1.741 ft	1.741 ft

time with the time step corresponding to the increment of 1° azimuth angle. The selections of the grids and time step are based on previous studies.[37]

The loosely coupled iterations are conducted in the following order. The flow simulation begins with a uniform freestream condition. In the first loose-coupling iteration, the CFD simulation proceeds for a full rotor revolution. The CFD loads for each blade computed in the fourth quarter of the revolution are used to obtain delta airloads[4] that are transferred to the CA solver. The CA solver uses the delta airloads to correct the internal lifting-line aerodynamics and compute the structural displacements. The structural displacements are used to update the CFD grid for the next loosely coupled iteration. In the subsequent loose-coupling iterations, the CFD simulations proceed one half of a rotor revolution before exchanging data with the CA solver. The CFD loads are computed in the second quarter of the half revolution. Rotor trimming is performed by the DYMORE5 quasisteady autopilot trimmer at each loose-coupling iteration to determine blade control pitch settings.

A. Hover Flight

The first set of flight conditions describe hover flights. Although zero-wind hover flow for isolated rotors can be more efficiently calculated using steady-state CFD in a noninertial reference frame,[10] the current verification and validation studies are conducted using the time-dependent loosely coupled FUN3D/DYMORE5 methodology. Three points on a thrust-sweep curve are computed at the solidity-weighted thrust levels of $C_T/\sigma = 0.05$, 0.07 and 0.09. The hub moment coefficients are set to zero. The hover flight with the thrust level of $C_T/\sigma = 0.07$ denoted as C9605 is assessed by loosely coupled FUN3D/DYMORE5 analyses on the coarse and fine grids. The fine grid is also used for predictions of the UH-60A hover performance for the thrust levels of $C_T/\sigma = 0.05$ and 0.09. The blade tip velocity and shaft tilt listed in Table 1 are kept fixed throughout all the hover-flight simulations.

A total of 23 loose-coupling iterations are performed, involving 12 rotor revolutions completed in the CFD simulations for each target thrust case. At the end of loose-coupling computations, converged trim targets, blade pitch controls, and airloads are established.

The FUN3D/DYMORE5 simulation on the fine grid provides the C9605-case Q-criterion data shown in Fig.3(a). Vorticity contours at a vertical plane cutting through the rotation center are also shown. Shed vortices are generated from inboard at the blade root and outboard at the blade tip and sweep break. Vortex rings convecting downward are clearly observed. As expected, vortices quickly dissipate after leaving the refined area of the background grid that extends only for $\pm 0.5R$ in the rotor-axis direction (Fig. 2(b)).

(a) Blade planform and radial stations with flight measurements

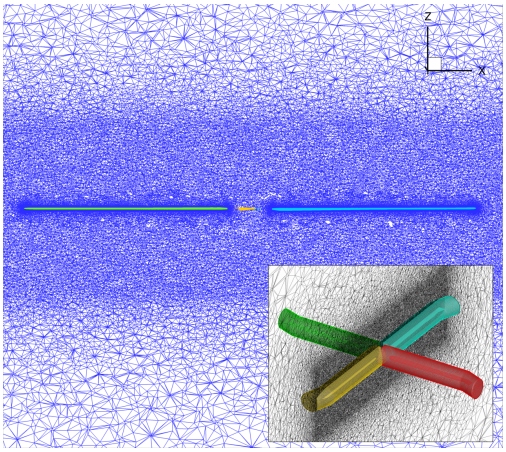

(b) Composite overset grid for four blades

Figure 2. UH-60A blade planform and coarse computational grid.

Figure 3(b) compares mean normal force distributions along the UH-60A blade. The mean normal forces, M^2C_n, correspond to averaged quantities from 360 azimuthal locations (one degree per time step) and are normalized by the speed of sound, freestream air density, and local airfoil chord length, c. The normal forces shown in Fig. 3(b) are normalized by the blade reference chord length (given in Table 1). Flight-test data are digitized from Ref. 4. The FUN3D/DYMORE5 solution on the fine grid captures the outboard peak loading slightly better than the solution from FUN3D/CAMRAD coupling. Overall, the agreement between the flight-test data and the computational solutions computed with the two different CA models is good. Compared to the fine-grid simulations, the coarse-grid FUN3D/DYMORE5 solution predicts airloads with a reasonable accuracy, except for some overpredictions near the sweep-break station.

Figure 4 compares the rotor performance obtained by FUN3D/DYMORE5 and FUN3D/CAMRAD analyses with flight-test data and with full-scale wind-tunnel data.[39] Figure 4(a) shows the rotor power for a range of thrust levels. The predictions of rotor performance by the FUN3D/DYMORE5 and FUN3D/CAMRAD analyses on the fine grid are in good agreement. The thrust values calculated from the FUN3D/DYMORE5 and FUN3D/CAMRAD simulations match well at all three thrust points considered; the maximum difference is less than 0.9% (max $\Delta C_T/\sigma \approx 0.0006$) for the median thrust condition. The numerical solutions show good correlations with the flight-test and wind-tunnel data. The coarse-grid FUN3D/DYMORE5 solution corresponding to the C9605 case ($C_T/\sigma = 0.07$) also predicts rotor performance qualitatively well considering the relatively few degrees of freedom used in the CFD simulation. Figure 4(b) shows comparisons of FMs computed by FUN3D/DYMORE5 and FUN3D/CAMRAD simulations. The FM is defined as,

$$\mathrm{FM} = \frac{C_T^{3/2}}{2\sqrt{C_P}}, \tag{17}$$

where C_P is the power coefficient. The maximum difference in FM is observed at the median thrust point and does not exceed 1% (max $\Delta\mathrm{FM} \approx 0.008$). Reference 40 shows that the use of the SA turbulence model together with the Delayed Detached Eddy Simulation (DDES) modeling improves the rotor-performance predictions. This variant will be considered in the future work.

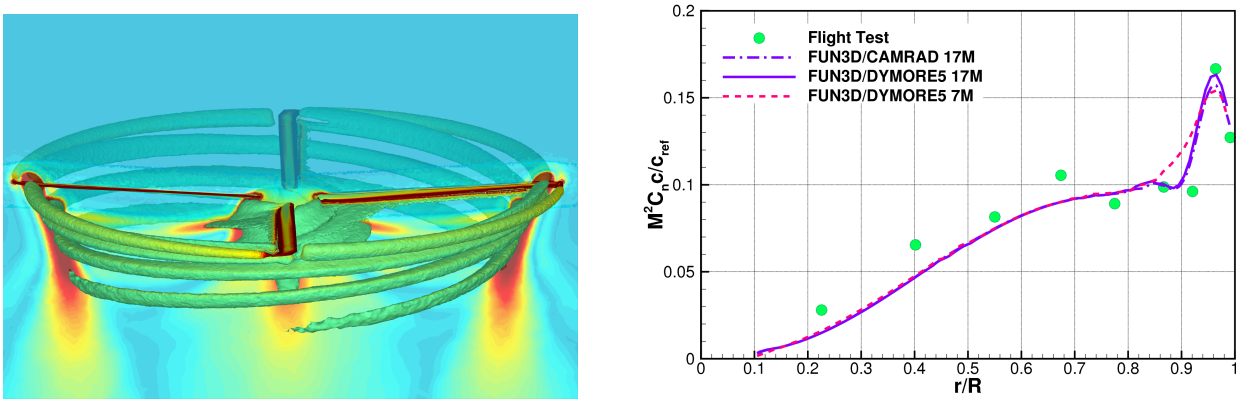

(a) Isosurfaces of q-criterion

(b) Comparison of mean normal force

Figure 3. Vorticity and airload distribution along UH-60A blade in hover flight (C9605).

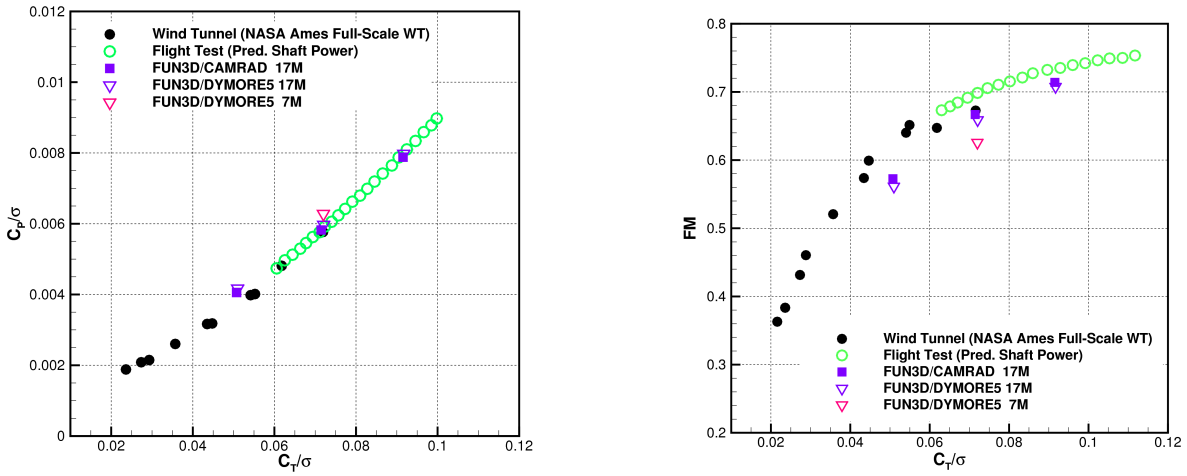

(a) C_P/σ vs. C_T/σ

(b) FM vs. C_T/σ

Figure 4. UH-60A hover-flight metrics for different thrust levels.

B. High-Speed Forward Flight

The second verification and validation study is conducted for the high-speed forward flight denoted as C8534. This flight condition represents the highest level-flight speed in the UH-60A Airloads Database. A total of 12 loose-coupling FUN3D/DYMORE5 iterations are performed, involving 7 revolutions of flow simulations. Variation of the control angles and thrust deltas between the 11^{th} and 12^{th} iterations is less than 0.001° and 2 lb (0.01%), respectively. Isosurfaces of q-criterion are shown in Fig. 5 near the flexible UH-60A rotor. The vortices are shed from the blade tip and near the sweep break. The vortices are convected primarily downstream of the rotor, and the blade-vortex interactions are not significant in this high-speed level-flight condition.

The loose-coupling FUN3D/DYMORE5 simulations for the C8534 case are compared to the FUN3D/CAMRAD simulations[37] and flight-test measurements. Figures 6 and 7 show comparisons of the sectional normal force and pitching moment coefficients, respectively. The sectional forces and moments computed by the CFD code include both pressure and skin-friction contributions, whereas the flight measurements only correspond to pressure contributions.

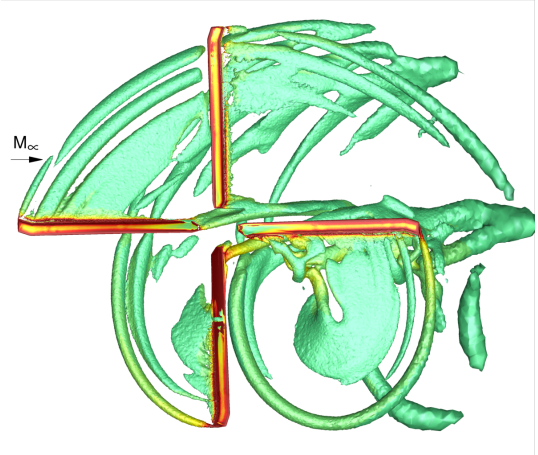

Figure 5. Isosurfaces of q-criterion near the flexible UH-60A rotor in high-speed forward flight (C8534). Contours are colored by magnitudes of vorticity.

The nondimensional normal forces and pitching moments, M^2C_n and M^2C_m, depicted in these figures are normalized by the speed of sound rather than the freestream velocity.

In comparison to the flight-test measurements, the computational analyses resolve reasonably well the magnitude and phases of the negative lift peak on the advancing side of the rotor disk at all blade stations; at a few locations, larger values of lift are observed in the FUN3D/DYMORE5 solution on the retreating side, e.g., in the third quadrant of outboard regions. Compared to the FUN3D/CAMRAD analysis, the FUN3D/DYMORE5 analysis shows slightly better predictions of negative peaks of the normal force at the outboard stations of $r/R = 0.775$, 0.865, 0.920, and 0.965, while the FUN3D/CAMRAD analysis better predicts forces on the retreating side of the rotor disk. Although the structural model parameters used in the DYMORE5 and CAMRAD solvers are similar, some differences in common parameters are observed. In addition, each CA solver has specific input parameters, which can lead to slightly different structural dynamics modeling. The maximum difference in the normal-force coefficient between the FUN3D/DYMORE5 and FUN3D/CAMRAD analyses is observed at the outboard station of $r/R = 0.965$ close to 110° and 210°, and is under 0.04. The FUN3D/DYMORE5 and FUN3D/CAMRAD simulations show somewhat better agreement in the predictions of sectional pitching moments. The maximum difference in the pitching-moment coefficient is observed close to 104° at the station of $r/R = 0.965$ and is under 0.003. Overall, the magnitudes and shapes of the normal-force and pitching-moment profiles predicted by the FUN3D/DYMORE5 solutions agree qualitatively well with those of the FUN3D/CAMRAD solutions. Loose-coupling FUN3D/DYMORE5 solutions computed on the coarse grid show a good agreement with the FUN3D/DYMORE5 solutions obtained on the fine grid.

VI. Multipoint Rotorcraft Design Optimization

In this section, the multidisciplinary sensitivity analysis is applied to gradient-based, constrained, multipoint optimization of the UH-60A Blackhawk helicopter blades.

A. General Design Setting

The order of design points can be arbitrary. For demonstration, the first design point is the hover flight C9605, and the second design point is the high-speed forward flight C8534. Flowfield quantities (such as Mach number), rotor operation parameters (such as advance ratio), and structure inputs are specified separately for each design point. Although different computational grids can be used at different design points, the coarse grid (7-million nodes) described in Section V is used at both the design points for the present optimization demonstration. The BDF2opt time integration scheme is used in FUN3D; the time step corresponds to 1° azimuth angle of rotor rotation. At each time step,

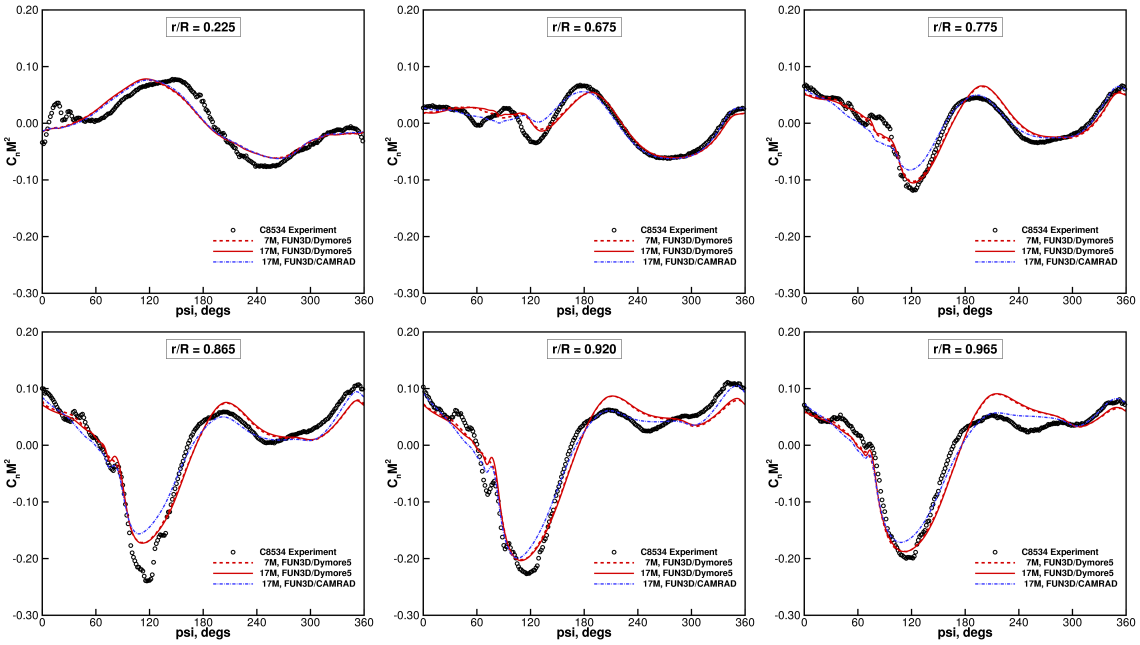

Figure 6. Sectional normal forces (means removed).

20 nonlinear subiterations are performed. The tolerance for the linear elasticity solver is set to 10^{-6}, which ensures reduction of six orders of magnitude in the root-mean-square norm of the residuals of the mesh-elasticity equations. The discretized flow equations (and flow-adjoint equations) are solved using a multicolor Gauss-Seidel point-implicit scheme, whereas the mesh elasticity equations (and grid-adjoint equations) are solved by the generalized minimum residual method[41] with a Gauss-Seidel point-implicit preconditioner. To avoid nonphysical deflections of the blades and alleviate the initial transient effects, FUN3D and DYMORE5 solutions are initialized with the loose-coupling FUN3D/DYMORE5 solutions obtained at the specific design points. The same initial conditions are used in every design cycle during the optimization process. Previous work[8] on a single-point design optimization of a HART-II rotorcraft configuration indicates that the loose-coupling initialization approach reduces the required simulation time and preserves the optimization quality.

B. Objectives and Constraints

The multipoint design optimization seeks to simultaneously maximize the rotorcraft figure of merit in hover flight and reduce the rotor power in forward flight for the UH-60A rotor system. Each design point targets certain thrust and rolling- and pitching-moment coefficients (see Table 1) as optimization constraints. The objective functions, f_i, and constraints, g_{1i}, g_{2i}, and g_{3i}, are defined in the following time-averaged forms:

$$f_i = w_{fi}\left[\left(\frac{1}{N_2-N_1+1}\sum_{n=N_1}^{N_2} C_{fi}^n\right) - C_{fi}^*\right]^2 \Delta t, \tag{18}$$

$$g_{1i} = w_{1i}\left[\left(\frac{1}{N_2-N_1+1}\sum_{n=N_1}^{N_2} C_{Ti}^n\right) - C_{Ti}^*\right]^2 \Delta t, \tag{19}$$

$$g_{2i} = w_{2i}\left[\left(\frac{1}{N_2-N_1+1}\sum_{n=N_1}^{N_2} C_{mxi}^n\right) - C_{mxi}^*\right]^2 \Delta t, \tag{20}$$

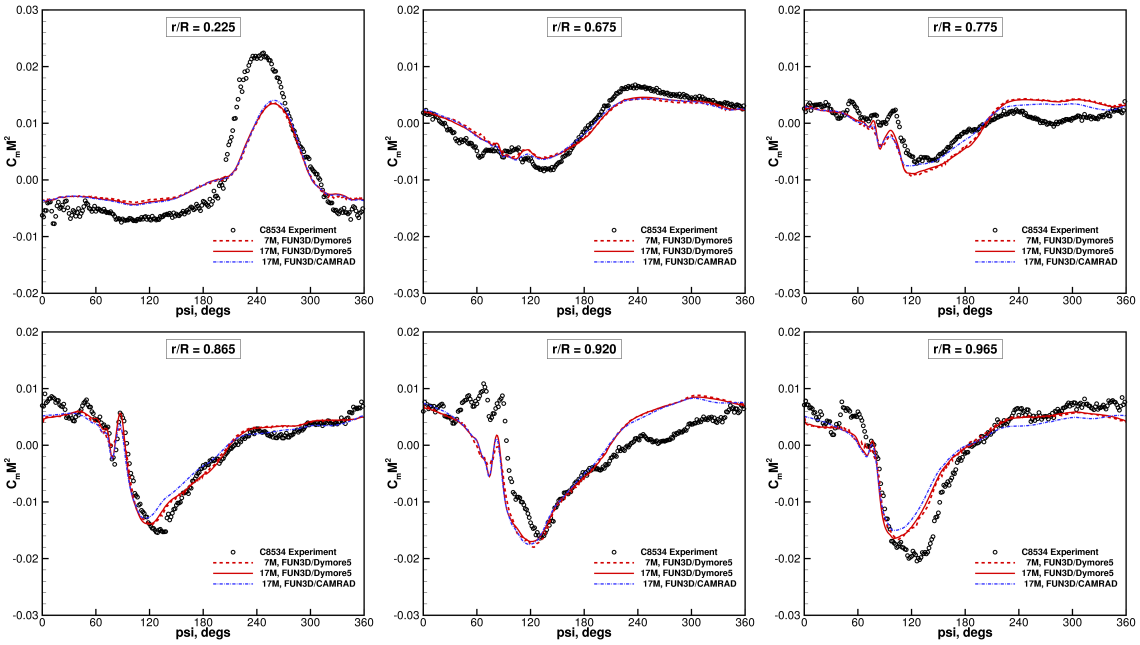

Figure 7. Sectional pitching moments (means removed).

$$g_{3i} = w_{3i}\left[\left(\frac{1}{N_2 - N_1 + 1}\sum_{n=N_1}^{N_2} C^n_{myi}\right) - C^*_{myi}\right]^2 \Delta t, \tag{21}$$

where i represents the design-point index. At the hover-flight (C9605) design point, the objective function, C_{f1}, is defined as:

$$C_{f1} = \mathrm{FM}^2 = \frac{C_T^3}{2C_P^2}. \tag{22}$$

This form of the objective function prevents negative thrusts from appearing under the square root. The target value $C^*_{f1} = 2$ exceeds the maximum objective-function value of 1. Coefficients C^*_{T1}, C^*_{mx1}, and C^*_{my1} are respective target values of rotor thrust and rolling- and pitching-moment coefficients; the values are specified in Table 1. At the forward-flight (C8534) design point, the objective function is defined as the rotor-power coefficient:

$$C_{f2} = C_P. \tag{23}$$

The target value of rotor power is $C^*_{f2} = 0$; the target values of thrust and rolling- and pitching-moment coefficients are provided in Table 1. The weighting parameters, w_{fi}, w_{1i}, w_{2i}, and w_{3i}, scale the objective and constraints at each individual design point and are specified based on the norms of sensitivity derivatives of the output functions corresponding to the baseline configuration. The weighting parameters, w_{f1} and w_{f2}, are specified to scale the objective functions to the same order of magnitude. Parameters N_1 and N_2 representing the first and last time-level indices of the optimization interval are set as $N_1 = 271$ and $N_2 = 360$, respectively. The optimization interval is the fourth quarter of the first rotor revolution.

A composite function, F_{mp}, is defined for a multipoint, multiobjective optimization problem. For the two-point design optimization case considered in the present study, F_{mp} is expressed as:

$$F_{mp} = a_1 f_1 + a_2 f_2, \tag{24}$$

where a_1 and a_2 are composite scaling parameters that are set to $a_1 = 5$ and $a_2 = 1$. A larger weighting for the hover design point than for the cruise design point is also reported in another multipoint design demonstration.[10]

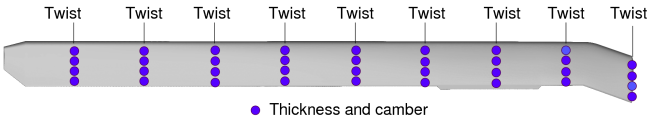

Figure 8. Locations of shape design parameters on UH-60A rotor blade.

C. Design Parameters

A geometry parameterization tool, Multidisciplinary Aerodynamic-Structural Shape Optimization Using Deformation (MASSOUD) software package,[42] is employed for surface grid deformation. MASSOUD uses a set of aircraft-centric shape design parameters such as planform, twist, shear, thickness, and camber to realize general configuration shape control. In the present demonstration, the set of design parameters consists of 81 shape parameters on the UH-60A rotor blades, including 9 twist parameters, 36 thickness parameters, and 36 camber parameters. The locations of twist, thickness, and camber shape design parameters on the UH-60A blades are illustrated in Fig. 8. The twist design variables are distributed at 9 radial stations. The thickness and camber are not allowed to be modified at the leading and trailing edges. The deviations of the shape design parameters from the baseline values are bounded within prescribed ranges. The bounds are specified to avoid nonphysical surface shapes. Each shape parameter is applied to all blades, producing identical blade shapes for the rotor system. In the multipoint design concept, the same shape parameters are used at all design points.

In addition, three control angles describing the collective and cyclic inputs are used as independent design parameters at each design point and are allowed to vary as much as ± 5 degrees. The control angles for the baseline configuration are initialized as the trim control angles computed by the loosely-coupled FUN3D/DYMORE5 system. Since the two design points correspond to distinct flight conditions, the trim control angles for the baseline configuration are different for the two design points. The quasisteady trimmer of the DYMORE5 model is not involved in the design optimization; the trim conditions are enforced by SNOPT as constraints on the thrust and rolling moment and pitching moment. The trim control angles computed by DYMORE5 and SNOPT are not identical as CA trimming is based on integration of forces and moments evaluated at airstations, whereas the SNOPT optimizer uses much finer CFD surface-grid resolution.

D. Optimization Results

The multipoint optimization demonstration has been performed on the NASA Advanced Supercomputing (NAS) facility's Pleiades supercomputer at the NASA Ames Research Center. Detailed computational cost breakdown for individual components of the design cycle is provided in Section VI.F. Figures 9(a) and 9(b) show convergence of the objectives and constraints for the hover- and forward-flight design points, respectively. An increase of 1.03% in the rotorcraft FM metric for the hover-flight condition, and a reduction of 3.91% in the rotor power for the forward-flight condition have been simultaneously achieved after 10 design cycles. A further increase in the FM metric at the hover point appears possible, considering the FM trend toward the end of design process. However, only 10 design cycles have been performed for the demonstration purpose. At the forward-flight design point, variation of the rotor power between the last two design cycles is relatively small.

Due to the fact that loose-coupling solutions are used as the initial conditions for the tight-coupling analysis, all initial constraints for the baseline configuration are close to the target values, as shown in Fig. 9. Table 2 lists the target values of constraints, the computed constraints from the baseline and optimized configurations, and deviations of the optimized configuration constraints from the targets. For example at the hover design point, the aerodynamic metrics computed from the first rotor revolution of the tight-coupling procedure agree well with the loose-coupling solutions. The thrust and rolling- and pitching-moment constraints of the optimized tight-coupling solutions further converge to the target values and provide better matches than the loose-coupling solutions of the baseline configuration. This further convergence is due to the use of forces and moments computed on CFD surface grid in the optimization, as opposed to forces and moments computed at airstations; the latter approach is commonly used by CA trimmer and produces small discrepancies in the computed thrust and moments between CFD and CA solutions. Similarly, at the

forward-flight design point, all optimized-configuration constraints achieve better matches with the targets than the baseline-configuration constraints.

Table 2. Thrust and rolling- and pitching-moment coefficients.

Design Point 1, Hover (C9605)				
Constraint	Target	Baseline	Optimized	Deviation from Target
C_T	5.819×10^{-3}	5.911×10^{-3}	5.822×10^{-3}	3.7×10^{-6}
C_{mx}	0	-2.645×10^{-7}	-3.946×10^{-8}	3.9×10^{-8}
C_{my}	0	-2.629×10^{-7}	-1.461×10^{-7}	1.5×10^{-7}

Design Point 2, Forward (C8534)				
Constraint	Target	Baseline	Optimized	Deviation from Target
C_T	6.701×10^{-3}	6.764×10^{-3}	6.738×10^{-3}	3.7×10^{-5}
C_{mx}	9.088×10^{-5}	5.592×10^{-5}	9.672×10^{-5}	5.8×10^{-6}
C_{my}	-6.271×10^{-5}	-5.162×10^{-5}	-5.475×10^{-5}	8.0×10^{-6}

Figure 10 depicts the convergence history of the collective and cyclic pitch control angles for the hover-flight and forward-flight design points. The initial control angles correspond to the loose-coupling trimmed solutions. Small deviations of the control angles from the initial values are observed during the entire optimization process. At the hover design point, the final collective control angle for the optimized UH-60A rotor is 8.2°. Compared to the loose-coupling solution, the collective control angle is increased by 1.8°. Although an increase in the collective control angle is obtained, the angular displacements about the blade axis, which account for combined rigid pitch controls and elastic torsion, are reduced by an average of 0.15° with the optimized configuration. This reduction of the angular displacements results in smaller pitch angles and a reduced rotor thrust, providing a better match with the target thrust value (c.f., Table 1). At the forward-flight design point, the final collective, lateral cyclic and longitudinal cyclic control angles for the optimized configuration are 10.0°, −1.29°, and −1.78°, respectively. The largest deviation

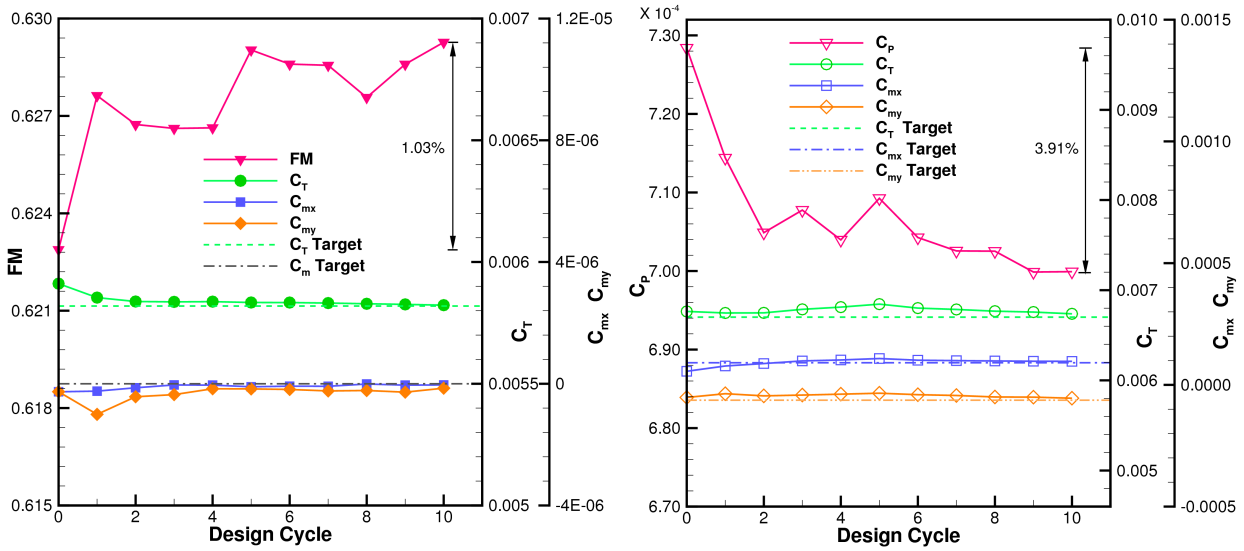

(a) Hover-flight design point

(b) Forward-flight design point

Figure 9. Convergence of objectives and constraints in UH-60A multipoint design optimization.

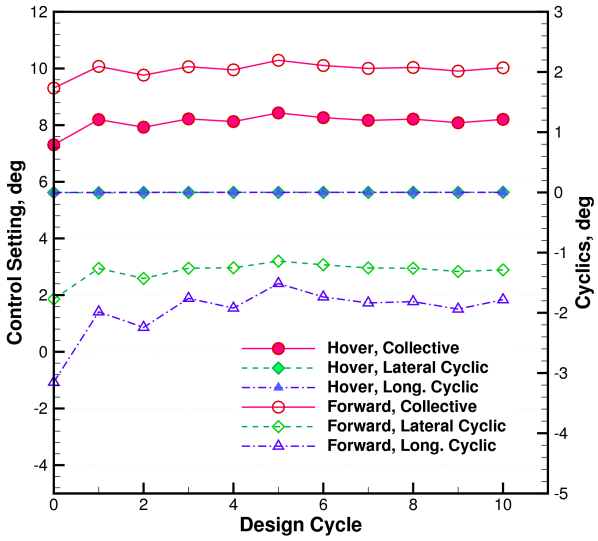

Figure 10. Variation of pitch control angles in UH-60A multipoint design optimization.

from the initial value, about 1.4°, is observed for the longitudinal cyclic angle. Overall, the optimized-configuration pitch-control angles are close to the loose-coupling baseline-configuration control angles. Note that the constraints on rotor thrust and moments restrict variation of the trim parameters.

Blade cross-section geometries of the baseline and optimized configurations are shown in Fig. 11 for spanwise stations ranging from 20% to 98% of the blade radius; an enlarged vertical scale (3:1) is used. The observed changes in the airfoil cross-sections are results of combined changes in many shape design parameters. The blade collective and cyclic pitch have been removed to allow comparison of the blade aerodynamic surfaces. Compared to the baseline shape, most notable changes in thickness occur outboard between the stations of 75% and 98%, particularly over the aft part of airfoil and near the midchord at the blade tip. In the midspan sections, a positive camber is observed in the front regions, and a negative camber is observed in the aft regions close to the trailing edge. The distribution of camber design parameters over the cross-section airfoil appear to vary gradually from inboard to outboard. Between the stations of 65% and 87%, a negative camber is observed in the front regions close to the leading edge, and a positive camber is observed in the aft regions. Close to the blade tip, a small negative camber is applied to almost the entire cross section. The optimized shape shows minor changes in the twist design parameters; a small negative twist (i.e., nose down) is applied outboard close to the 87%-station.

E. Long-term Tight-coupling Assessment

The multipoint optimization procedure demonstrated in this paper uses the fourth quarter of the first rotor revolution as the optimization time interval for both the design points. The use of loose-coupling solutions for initialization of the flow and CA solutions alleviates the initial transient effects. However, the transient effects cannot be fully eliminated. The initial loose-coupling solutions correspond to the periodic solutions associated with the baseline geometry and are not updated in the design process. The optimized configuration has blades of different shape and uses different pitch control parameters. If the changes are large, the initial transients may significantly affect solutions within the optimization time interval. To assess viability of optimization benefits for periodic solutions, long-term tightly coupled FUN3D/DYMORE5 simulations are performed for both the baseline and optimized configurations

Figure 12(a) shows time histories of the FM, thrust and rolling- and pitching-moment coefficients for the baseline and optimized configurations obtained by the tight-coupling hover-flight FUN3D/DYMORE5 simulations. Ten revolutions are simulated. Figures 12(b) and 12(c) show forward-flight time histories of the rotor power coefficient and the thrust, rolling-moment, and pitching-moment coefficients, respectively. These long-term simulations assess optimization benefits in the limit of a periodic solution. The coupled FUN3D/DYMORE5 solutions at both the design points

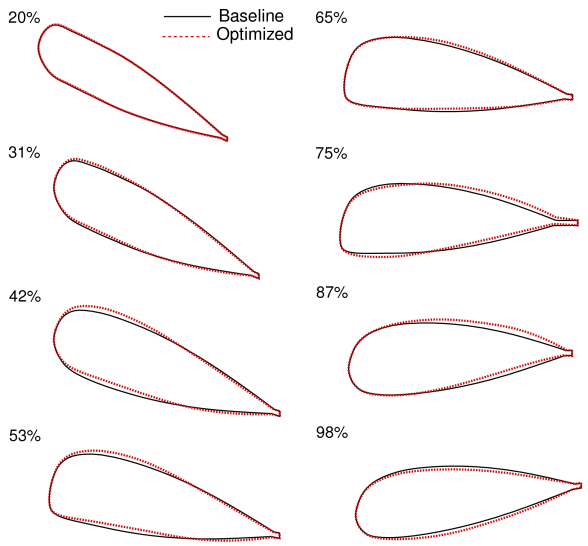

Figure 11. Baseline and optimized blade section geometries in exaggerated vertical scale ($y : z = 1 : 3$).

are quickly settled; periodic solutions are established shortly after the first rotor revolution. The influence of initial transients appears to be less significant on the forward flight than on the hover flight. This is possibly due to relatively slower development of the flow wake in the hover-flight case. The long-term simulations indicate that the rotor performance benefits including FM and rotor power have been preserved or somewhat enhanced in the periodic-solution regimes. Comparing the tenth revolution of the optimized rotor configuration with the baseline, the hover-flight FM is increased by 1.37%, and the forward-flight rotor power is decreased by 3.98%; both numbers are better than the numbers shown in Fig. 9. The mean values of thrust, rolling moment and pitching moment at both design points are preserved, indicating that the required trim conditions have been well maintained.

Note that the coarse grid is used at the hover and forward-flight design points for a demonstration of the multidisciplinary, multipoint, design and optimization capabilities. As a finer-resolution grid is considered, the design optimization procedure may introduce variations to the final optimized configuration. However, such a coarse-grid shape optimization is still beneficial to provide important guidance for a fine-grid design and optimization and helps to accelerate the overall optimization convergence.

F. Computational Cost of Design Optimization

The multipoint optimization demonstration has been performed on 2136 Broadwell processing cores. The multidisciplinary FUN3D/DYMORE5 analysis and sensitivity analysis at each design point use all available processing cores. In this computation environment, execution of the two-point optimization cycle requires 12.2 hours of wall-clock time. Considering two design points, a total of 2 multidisciplinary CFD/CA solutions evaluating 8 design functions and 8 multidisciplinary adjoint solutions are computed at each design cycle. A breakdown of the time usage within the design cycle is provided in Table 3. The total wall-clock times used to solve the tightly coupled CFD/CA analysis equations, the load adjoint equations, and the CFD (flow and grid) adjoint equations are shown separately in the table as well as the percentage of time spent on solutions of particular sets of equations. Each individual component spends about the same time in each of the two design points. The total time for computing adjoint solutions is a factor of 3.5 greater than the time for computing the CFD/CA analysis solution. One reason for the higher cost of the multidisciplinary sensitivity analysis is the need to compute, for each design point, four adjoint solutions corresponding to one objective and three constraints. Another reason is that the computational time required to compute complex-variable grid sensitivities to airloads (involving DYMORE5 sensitivities) grows quadratically with the number of time steps (see Equations (11)–(15)). This quadratic dependence affects the time of computing load adjoint solutions.

For the current design optimization case, the cost of computing complex-variable DYMORE5 sensitivities and the

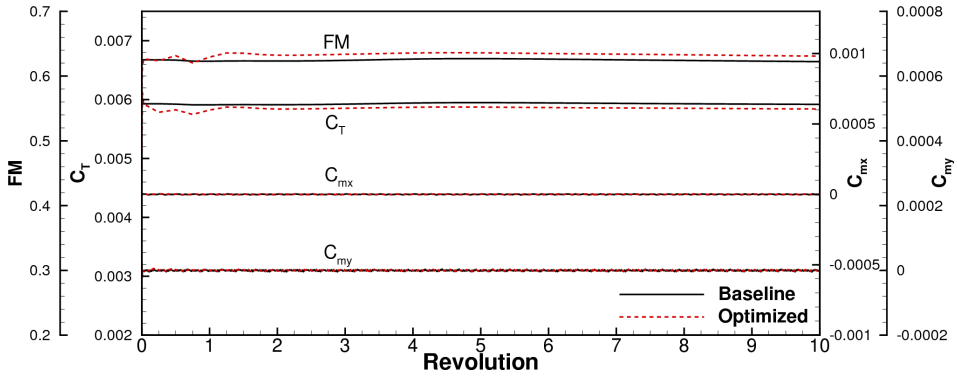

(a) Objective and constraints at hover-flight point

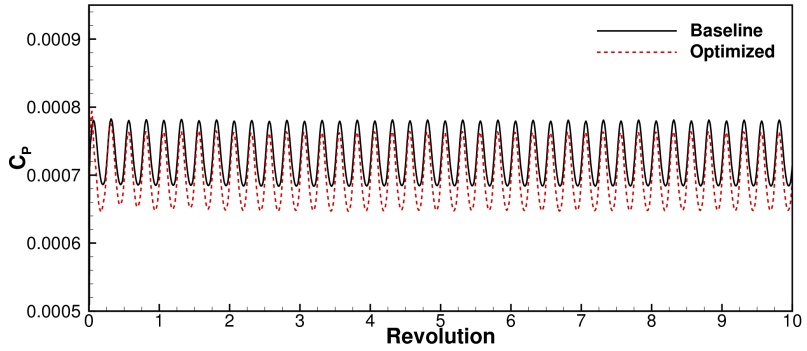

(b) Objective at forward-flight point

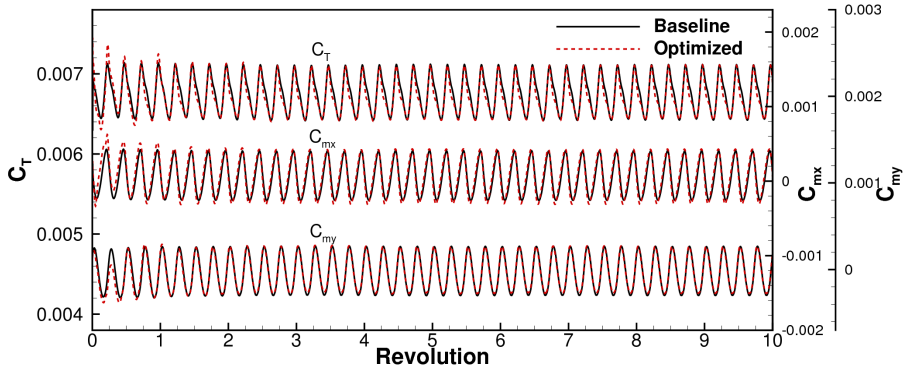

(c) Constraints at forward-flight point

Figure 12. Long-term tight-coupling simulations of baseline and optimized configurations.

resulting grid-motion sensitivities is 23% of the total cost and 42% of the CFD adjoint cost. This multidisciplinary rotorcraft optimization performance is acceptable in a high-performance computing environment. For problems requiring a long integration or fine resolution in time, such as maneuvering-flight cases, the cost for complex-variable DYMORE sensitivities will become dominant because of the quadratic dependence. A discretely-consistent adjoint formulation is required for the CA model to completely eliminate this quadratic dependence and improve the overall performance of gradient-based CFD/CA design optimization. A separate effort is currently underway to develop adjoint capabilities in the DYMORE solver.[43]

Table 3. Two-point design cycle breakdown (2136 processors).

Component	Wall-clock time (h)	Percent (%)
CFD/CA analyses	2.7	22.2
Load adjoint	2.8	23.0
CFD adjoint	6.7	54.8

VII. Conclusions

This paper presents a multidisciplinary, multipoint, gradient-based design and optimization for high-fidelity rotorcraft simulations conducted by a tightly-coupled system including a computational fluid dynamics code, FUN3D, and a rotorcraft comprehensive analysis code, DYMORE5. A formulation for the tight-coupling multidisciplinary sensitivity analysis has been developed and implemented. The formulation integrates the adjoint-based sensitivities of flow and grid solutions available in FUN3D with DYMORE5 sensitivities computed by a complex-variable perturbation approach.

The multidisciplinary rotorcraft analysis is verified and validated for an isolated UH-60A Blackhawk rotor in hover and high-speed forward flight. The FUN3D/DYMORE5 solutions compare well with simulations obtained from an established FUN3D/CAMRAD analysis and a flight-test database. A constrained, gradient-based, multipoint design optimization procedure has been formulated and successfully applied to optimization of the UH-60A rotor blades, simultaneously optimizing both hover and forward flights. The demonstration comprised the objectives of increasing the rotorcraft figure of merit in hover flight and reducing the rotor power in forward flight while maintaining baseline thrust, rolling moment and pitching moment for specified flight conditions. The optimized configuration produced improvements in both flight conditions. The improved rotor performance metrics are well preserved in the periodic-solution regimes, and all constraints are also maintained. This demonstration confirms the feasibility and effectiveness of the current high-fidelity, multidisciplinary sensitivity analysis for rotorcraft applications. The computational cost for the multidisciplinary multipoint design optimization has been analyzed for the FUN3D/DYMORE5 system and found affordable for optimization of level-flight periodic rotorcraft conditions. Ongoing work is conducted on development of discretely-consistent adjoint capabilities in DYMORE to extend the high-fidelity optimization framework to long-time simulations of maneuvering rotorcraft.

Acknowledgments

The work was supported by the NASA Revolutionary Vertical Lift Technology, NASA Activity 201093. The authors would like to thank William Jones at NASA Langley Research Center for assistance with geometry parameterization.

References

[1]Saberi, H., Khoshlahjeh, M., Ormiston, R. A., and Rutkowski, M. J., "Overview of RCAS and Application to Advanced Rotorcraft Problems," Jan. 2004, American Helicopter Society 4th Decennial Specialists Conference on Aeromechanics.

[2]Johnson, W., *Rotorcraft Aeromechanics*, Cambridge Aerospace Series, Cambridge University Press, 2013, doi:10.1017/CBO9781139235655.

[3]Bauchau, O. A., Bottasso, C. L., and Nikishkov, Y. G., "Modeling Rotorcraft Dynamics with Finite Element Multibody Procedures," *Mathematical and Computer Modeling*, Vol. 33, 2001, pp. 1113–1137, doi:10.1016/S0895-7177(00)00303-4.

[4]Potsdam, M., Yeo, H., and Johnson, W., "Rotor Airloads Prediction Using Loose Aerodynamic/Structural Coupling," *Journal of Aircraft*, Vol. 43, No. 3, 2006, pp. 732–742, doi:10.2514/1.14006.

[5]Biedron, R. T. and Lee-Rausch, E. M., "Rotor Airloads Prediction Using Unstructured Meshes and Loose CFD/CSD Coupling," June 2008, AIAA Paper 2008–7341.

[6]Sitaraman, J., Potsdam, M., Jayaraman, B., Datta, A., Wissink, A., Mavriplis, D., and Saberi, H., "Rotor Loads Prediction Using Helios: A Multi-Solver Framework for Rotorcraft CFD/CSD Analysis," Jan. 2011, AIAA Paper 2011–1123.

[7]Smith, M. J., Lim, J. W., van der Wall, B. G., Baeder, J. D., Biedron, R. T., Boyd Jr., D. D., Jayaraman, B., Jung, S. N., and Min, B.-Y.,

"The HART II International Workshop: An Assessment of the State of the Art in CFD/CSD Prediction," *CEAS Aeronautical Journal*, Vol. 4, 2013, pp. 345–372, doi:10.1007/s13272-013-0078-8.

[8]Wang, L., Diskin, B., Biedron, R. T., Nielsen, E. J., Sonneville, V., and Bauchau, O. A., "High-Fidelity Multidisciplinary Design Optimization Methodology with Application to Rotor Blades," Jan. 2018, American Helicopter Society International Technical Meeting, Aeromechanics Design for Transformative Vertical Flight.

[9]Nielsen, E. J. and Diskin, B., "Discrete Adjoint-Based Design for Unsteady Turbulent Flows on Dynamic Overset Unstructured Grids," *AIAA Journal*, Vol. 51, No. 6, 2013, pp. 1355–1373, doi:10.2514/1.J051859.

[10]Jones, W. T., Nielsen, E. J., Lee-Rausch, E. M., and Cecil W. Acree, J., "Multi-point Adjoint-Based Design of Tilt-Rotors in a Noninertial Reference Frame," Jan. 2014, AIAA Paper 2014–0290.

[11]Mavriplis, D. J., Fabiano, E., and Anderson, E., "Recent Advances in High-Fidelity Multidisciplinary Adjoint-Based Optimization with the NSU3D Flow Solver Framework," Jan. 2017, AIAA Paper 2017–1669.

[12]Wang, L., Diskin, B., Biedron, R. T., Nielsen, E. J., and Bauchau, O. A., "Sensitivity Analysis of Multidisciplinary Rotorcraft Simulations," Jan. 2017, AIAA Paper 2017–1670.

[13]Wang, L., Diskin, B., Biedron, R. T., Nielsen, E. J., and Bauchau, O. A., "High-Fidelity Multidisciplinary Sensitivity Analysis and Design Optimization for Rotorcraft Applications," AIAA Journal, Accepted.

[14]Boopathy, K. and Kennedy, G. J., "Adjoint-based Derivative Evaluation Methods for Flexible Multibody Systems with Rotorcraft Applications," Jan. 2017, AIAA Paper 2017–1671.

[15]Biedron, R. T., Carlson, J.-R., Derlaga, J. M., Gnoffo, P. A., Hammond, D. P., Jones, W. T., Kleb, B., Lee-Rausch, E. M., Nielsen, E. J., Park, M. A., Rumsey, C. L., Thomas, J. L., and Wood, W. A., "FUN3D Manual: 13.3," NASA/TM-2018-219808, NASA Langley Research Center, Hampton, VA, 2018.

[16]Newman III, J. C., Anderson, W. K., and Whitfield, D. L., "Multidisciplinary Sensitivity Derivatives Using Complex Variables," July 1998, Computational Fluid Dynamics Laboratory, NSF Engineering Research Center for Computational Field Simulation, MSSU-COE-ERC-98-08, 1998.

[17]Wang, L., Diskin, B., Biedron, R. T., Nielsen, E. J., Sonneville, V., and Bauchau, O. A., "High-Fidelity Multidisciplinary Design Optimization Methodology with Application to Rotor Blades," Aug. 2018, Journal of the American Helicopter Society, Under review.

[18]Sonneville, V., Cardona, A., and Brüls, O., "Geometrically Exact Beam Finite Element Formulated on the Special Euclidean Group SE(3)," *Computer Methods in Applied Mechanics and Engineering*, Vol. 268, No. 1, 2014, pp. 451–474, doi:10.1016/j.cma.2013.10.008.

[19]Sonneville, V. and Brüls, O., "A Formulation on the Special Euclidean Group for Dynamic Analysis of Multibody Systems," *Journal of Computational and Nonlinear Dynamics*, Vol. 9, No. 4, 2014, pp. 041002, doi:10.1115/1.4026569.

[20]Sonneville, V. and Bauchau, O. A., "Parallel Implementation of Comprehensive Rotor Dynamics Simulation based on the Motion Formalism," 2017, American Helicopter Society 73rd Annual Forum.

[21]Lee-Rausch, E. M. and Biedron, R. T., "FUN3D Airload Predictions for the Full-Scale UH-60A Airloads Rotor in a Wind Tunnel," May 2013, American Helicopter Society 69th Annual Forum.

[22]Nielsen, E. J., "Adjoint-Based Aerodynamic Design of Complex Aerospace Configurations," July 2016, ASME 2016 Fluids Engineering Division Summer Meeting, FEDSM 2016–7573.

[23]Nielsen, E. J. and Diskin, B., "High-Performance Aerodynamic Computations for Aerospace Applications," *Parallel Computing*, Vol. 64, 2017, pp. 20–32, doi:10.1016/j.parco.2017.02.004.

[24]Roe, P. L., "Approximate Riemann Solvers, Parameter Vectors, and Difference Schemes," *Journal of Computational Physics*, Vol. 43, No. 2, 1981, pp. 357–372, doi:10.1016/0021-9991(81)90128-5.

[25]Burg, C. O. E., "Higher Order Variable Extrapolation For Unstructured Finite Volume RANS Flow Solvers," June 2005, AIAA Paper 2005–4999.

[26]van Leer, B., "Towards the Ultimate Conservative Difference Scheme, V. A Second Order Sequel to Godunov's Method," *Journal of Computational Physics*, Vol. 32, No. 1, 1979, pp. 101–136, doi:10.1016/0021-9991(79)90145-1.

[27]Haselbacher, A. and Blazek, J., "Accurate and Efficient Discretization of Navier-Stokes Equations on Mixed Grids," *AIAA Journal*, Vol. 38, No. 11, 2000, pp. 2094–2102.

[28]Vatsa, V., Carpenter, M. H., and Lockard, D., "Re-evaluation of An Optimized Second Order Backward Difference (BDF2OPT) Scheme for Unsteady Flow Applications," Jan. 2010, AIAA Paper 2010–0122.

[29]Noack, R., "DiRTlib: A Library to Add an Overset Capability to Your Flow Solver," June 2005, AIAA Paper 2005–5116.

[30]Noack, R., Bogar, D., Kunz, R., and Carrica, P., "SUGGAR++: An Improved General Overset Grid Assembly Capability," June 2009, AIAA Paper 2009–3992.

[31]Anderson, W. K., Newmann, J. C., Whitfield, D. L., and Nielsen, E. J., "Sensitivity Analysis for Navier-Stokes Equations On Unstructured Meshes Using Complex Variables," *AIAA Journal*, Vol. 39, No. 1, 2001, pp. 56–63.

[32]Martins, J. R. R. A., Kroo, I. M., and Alonso, J. J., "An Automated Method For Sensitivity Analysis Using Complex Variables," Jan. 2000, AIAA Paper 2000–0689.

[33]Abras, J. N., Lynch, C. E., and Smith, M. J., "Computational Fluid Dynamics-Computational Structural Dynamics Rotor Coupling Using an Unstructured Reynolds-Averaged Navier-Stokes Methodology," *Journal of the American Helicopter Society*, Vol. 57, No. 012001, 2012, pp. 1–14, doi:10.4050/JAHS.57.012001.

[34]Nielsen, E. J. and Anderson, W. K., "Recent Improvements in Aerodynamic Design Optimization on Unstructured Meshes," *AIAA Journal*, Vol. 40, No. 6, 2001, pp. 1155–1163, doi:10.2514/2.1765.

[35]Gill, P. E., Murray, W., and Saunders, M. A., "SNOPT: An SQP Algorithm for Large-Scale Constrained Optimization," *SIAM Journal on Optimization*, Vol. 12, No. 4, 2002, pp. 979–1006.

[36]Gill, P. E., Murray, W., and Saunders, M. A., "SNOPT: An SQP Algorithm for Large-Scale Constrained Optimization," *SIAM Review*, Vol. 47, No. 1, 2005, pp. 19–131, doi:10.1137/S0036144504446096.

[37]Biedron, R. T. and Lee-Rausch, E. M., "Computation of UH-60A Airloads Using CFD/CSD Coupling On Unstructured Meshes," May 2011, American Helicopter Society 67th Annual Forum.

[38]Spalart, P. and Allmaras, S., "A one-equation Turbulence Model for Aerodynamic Flows," *Le Recherche Aerospatiale*, Vol. 1, 1994, pp. 5–21, doi:10.2514/6.1992-439.

[39]Shinoda, P. M., Yeo, H., and Norman, T. R., "Rotor Performance of a UH-60 Rotor System in the NASA Ames 80- by 120-Foot Wind Tunnel," June 2002, American Helicopter Society 58th Annual Forum.

[40]Chaderjian, N. M. and Ahmad, J. U., "Detached Eddy Simulation of the UH-60 Rotor Wake Using Adaptive Mesh Refinement," May 2012, American Helicopter Society 68th Annual Forum.

[41]Saad, Y. and Schultz, M. H., "GMRES: A Generalized Minimal Residual Algorithm for Solving Nonsymmetric Linear Systems," *SIAM Journal on Scientific Computing*, Vol. 7, No. 3, 1996, pp. 856–869, doi:10.1137/0907058.

[42]Samareh, J. A., "Novel Multidisciplinary Shape Parameterization Approach," *Journal of Aircraft*, Vol. 38, No. 6, 2001, pp. 1015–1024, doi:10.2514/2.2888.

[43]Callejo, A., Sonneville, V., and Bauchau, O., "Discrete Adjoint Method for the Sensitivity Analysis of Flexible Multibody Systems," *Journal of Computational and Nonlinear Dynamics*, 2018, doi:10.1115/1.4041237, Available online.